Research Article | Vol. 10, No. 11 / 1 November 2019 / Biomedical Optics Express 5724

Biomedical Optics EXPRESS

Clinical multi-functional OCT for retinal imaging

SHINNOSUKE AZUMA,[1,4] SHUICHI MAKITA,[1,4] DEEPA KASARAGOD,[1,4] SATOSHI SUGIYAMA,[2] MASAHIRO MIURA,[3,4] AND YOSHIAKI YASUNO[1,4,*]

[1] Computational Optics Group, University of Tsukuba, 1–1–1 Tennodai, Tsukuba, Ibaraki 305–8573, Japan
[2] Tomey Corporation, Nagoya, Aichi 451–0051, Japan
[3] Tokyo Medical University Ibaraki Medical Center, 3–20–1 Chuo, Ami, Ibaraki 300–0395, Japan
[4] Computational Optics and Ophthalmology Group, Tsukuba, Ibaraki 305–8531, Japan
[*] yasuno@optlab2.bk.tsukuba.ac.jp
http://optics.bk.tsukuba.ac.jp

Abstract: A compact clinical prototype multi-functional optical coherence tomography (OCT) device for the posterior human eye has been developed. This compact Jones-matrix OCT (JM-OCT) device integrates all components into a single package. Multiple image functions, i.e., scattering intensity, OCT angiography, and the degree of polarization uniformity, are obtained. The device has the capability for measuring local birefringence. Multi-functional imaging of several eyes with age-related macular degeneration is demonstrated. The compact JM-OCT device will be useful for the *in vivo* non-invasive investigation of abnormal tissues.

1. Introduction

Optical coherence tomography (OCT) [1] is a non-invasive biomedical imaging modality that can provide high-contrast cross-sectional and volumetric images. Several aspects of OCT technology have been developed such as measurement speed, sensitivity, resolution, and functional extension. Among these aspects, measurement speed and sensitivity have been significantly enhanced by Fourier-domain OCT. Although Fourier-domain OCT enables high-contrast three-dimensional imaging, it provides only an intensity-based image that visualizes tissue structure by employing the intensity of backscattered light. Several functional extensions have been developed to enable the investigation of other properties of tissues.

OCT angiography (OCTA) is a recently developed technology and has been rapidly adapted for ophthalmology. The first *in vivo* non-invasive OCT based angiography, which was based on Doppler OCT, was demonstrated in 2006 [2]. After this first demonstration, several OCTA methods have been developed, such as phase variance [3,4], intensity correlation [5–7], and complex-based algorithms [8–10]. The clinical utility of OCTA was investigated in several diseases including age-related macular degeneration (AMD) [11], diabetic retinopathy [12,13], and glaucoma [14]. As the clinical utility of OCTA has become widely accepted in ophthalmology, OCTA functionality has been integrated into state-of-the-art commercial OCT devices.

Polarization-sensitive OCT is another functional extension that contrasts tissues with polarization properties, such as phase retardation [15,16] and the randomness of the polarization state such as degree of polarization uniformity (DOPU) [17]. In ophthalmology, various clinical studies for both anterior [18–21] and posterior [22–27] segments of the eye have been reported. Among several subtypes of polarization-sensitive OCT, Jones-matrix OCT (JM-OCT) can obtain polarization properties with simple single-mode-fiber optics [28–31]. This approach obtains the Jones matrix of the optical system including the tissues from an input polarization state separator (or modulator) to a polarization detector. The polarization properties of the tissues are then extracted from the Jones matrix. There are several derivative methods for extracting polarization properties such as those that use the Müller–Jones matrix [32–35] or covariance matrix [36].

#373211 https://doi.org/10.1364/BOE.10.005724
Journal © 2019 Received 19 Jul 2019; revised 1 Oct 2019; accepted 2 Oct 2019; published 14 Oct 2019

Biomedical Optics EXPRESS

Recently developed retinal multi-functional OCT simultaneously visualizes scattering intensity, blood flow, and polarization properties. In 2012, swept-source based JM-OCT, which consists of only passive optical components, was developed [37,38], one of which enables the simultaneous imaging of multiple properties [37]. Ju *et al.* also developed an advanced prototype of JM-OCT [39], and they demonstrated the simultaneous measurement of sensitivity-enhanced intensity, power of Doppler shift, DOPU, and cumulative phase retardation. In 2014, an investigation to the imaging of exudative AMD using this JM-OCT prototype was reported. This device simultaneously visualized vasculature abnormalities, retinal pigment epithelium (RPE) defects, and fibrotic lesions [25].

Several clinical-grade retinal multi-functional OCT have been demonstrated. We developed the first clinical JM-OCT device [40] that was designed to operate in a clinic. Local birefringence imaging of the posterior part of the eye was demonstrated with both normal and pathologic subjects. In addition to this fully functional JM-OCT device, a simplified clinical-grade multi-functional OCT device was developed [41]. This simplified multi-functional OCT has all image functions except for birefringence. The reduction of birefringence measurement capability eliminates the requirement of input-polarization multiplexing. Hence, this simplified multi-functional OCT is as compact as a commercially available OCT device.

Several clinical studies using clinical multi-functional OCT prototypes have been reported [27,42,43]. The images of multiple properties obtained by JM-OCT can be used to generate "synthetic images." For example, the recently presented composite *en face* image projection combining OCTA and DOPU is suitable for detecting RPE damage and abnormal vasculature simultaneously [41]. Another example of image synthesis is the generation of a tissue-specific image. For instance, an RPE-melanin image can be generated by synthesizing attenuation, OCTA, and DOPU images obtained by JM-OCT [44]. This approach enables easier and more comprehensive interpretation of JM-OCT data [43]. Hence, JM-OCT is a promising modality for clinical applications.

In this paper, we further develop a clinical JM-OCT device that provides multiple image functions including conventional scattering intensity, OCTA, DOPU, and birefringence. The clinical-grade JM-OCT device was developed by integrating the system components of swept-source OCT and additional components for Jones matrix measurements in a retinal scanning unit. This developed device achieves a compact footprint by employing encapsulated optical modules. However, the compact packing of the device resulted in an undesired elevation in temperature of fiber couplers that destabilized the optical power of the probe beam. This issue has been resolved by using a temperature-stabilized fiber component. The clinical utility of the developed JM-OCT device is demonstrated by measuring pathologic subjects.

2. Clinical-grade posterior eye Jones-matrix optical coherence tomography

2.1. System configuration

A schematic diagram of the developed clinical posterior JM-OCT device using the passive-component-based JM-OCT method [37–40,45] is shown in Fig. 1. The optical system of the interferometer, which is built with single-mode optical fibers, consists of a variable reference delay line (150-mm optical distance, VDL–06–50–SM, Advanced Fiber Resources, Hong Kong), a retinal scanning unit, and two optical modules. One of the modules is a passive polarization delay module (PDM; DE–G043–10, Optohub Co. Ltd., Saitama, Japan), which separates an input light into two orthogonal polarization states and applies a delay between them. The other is a polarization-diversity and coherent-detection module (PDCDM; DE–G036–10, Optohub Co. Ltd., Saitama, Japan), which makes the light from two input ports interfere, splits orthogonal polarization states, and converts the interference signal to an electric signal using two balanced photo detectors.

Biomedical Optics EXPRESS

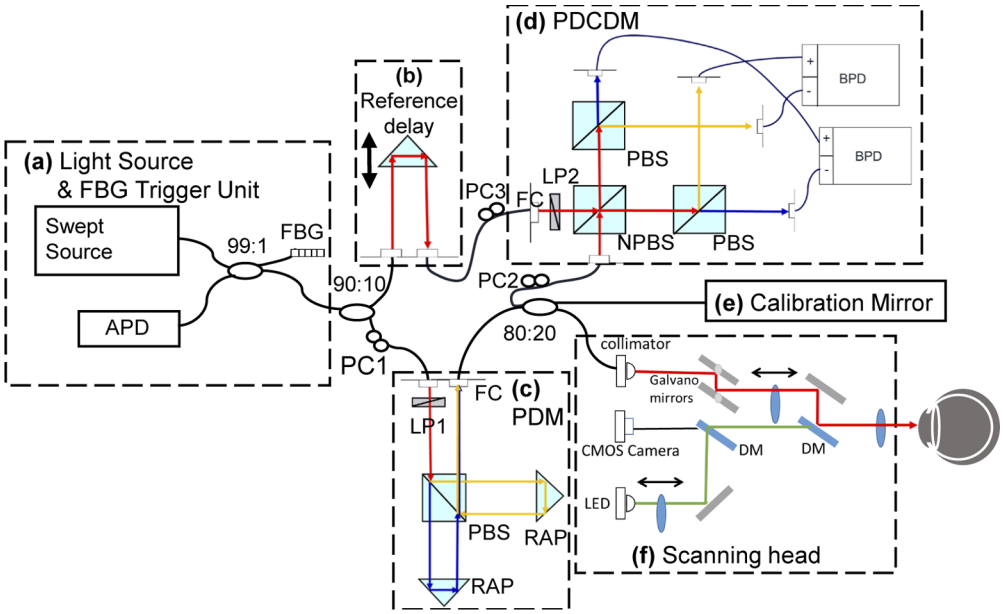

Fig. 1. Schematic diagram of the developed JM-OCT device. (a) Light source and FBG trigger unit, (b) reference delay, (c) passive polarization delay module (PDM), (d) polarization-diversity and coherent-detection module (PDCDM), (e) calibration mirror, and (f) scanning head. FBG: fiber Bragg grating, APD: avalanche photo detector, BPD: balanced photo detector, DM: dichroic mirror, FC: fiber collimator, LP1, LP2: linear polarizers, NPBS: non-polarizing beam splitter, PBS: polarizing beam splitter, PC1, PC2, PC3: polarization controllers, and RAP: right-angle prism.

Light is emitted from the wavelength sweeping light source with a scanning frequency of 100 kHz (AXP50124–3, Axsun Technologies, MA, USA) and goes into a 99:1 coupler. The 1 % part of the light is directed to the fiber Bragg grating (FBG). The light of a certain wavelength is reflected by the FBG, hence, it is a good signature of the temporal timing of a wavelength sweep. The light reflected from the FBG is detected by an avalanche photodiode (APD), and this signal is used as a trigger for each wavelength sweep acquisition.

The remaining 99 % of the light from the 99:1 coupler is divided by a 90:10 fiber coupler. The 90 % portion of the light is directed into the PDM of the probe arm. By passing through the PDM, two orthogonal incident polarization states are multiplexed with respect to optical path length. The light from the output port of the PDM is then split by an 80:20 coupler. The 80 % portion of the light is directed to the phase calibration mirror, which is used to reflect and provide the phase calibration signal to the detectors [39].

The remaining 20 % portion of the light is guided into the probe arm where the optical fiber is connected to a retinal scanning unit. The retinal scanning unit consists of a two-axis galvanometric scanning mirror, which is controlled by a multifunctional I/O device (PCIe-6323, National Instruments, TX, USA), a complementary metal-oxide-semiconductor (CMOS) image sensor for monitoring the pupil of the subject, a fixation target made with a matrix LED panel for guiding the subject's eye, a motorized focusing lens, and a motorized alignment stage. The power of the probe beam is 1.4 mW on the cornea, which satisfies the safety standard defined by the American National Standards Institute [46].

The backscattered light from the sample and calibration signal are recoupled by the 80:20 coupler, and the 80 % portion of the light is directed to a PDCDM. The backscattered probe beam

Biomedical Optics EXPRESS

and reference beam are recoupled in the PDCDM, and two orthogonal polarization components are independently detected by built-in balanced detectors.

The two output signals of the PDCDM pass through 1-MHz high pass filters and 250-MHz low pass filters (HP1CH3–0S and LP250CH3–0S, 7th–order type–I Chebyshev, R & K, Shizuoka, Japan) and are directed into two analog input channels of the digitizer (ATS9350, Alazar Technologies Inc., Quebec, Canada). The analog input signals are digitized at 12-bit resolution with a sampling rate of 500 MS/s using an internal clock of the digitizer. Each spectrum is sampled with 2,560 sampling points per wavelength scan.

The sensitivity of each polarization channel has been measured and the average of sensitivities is 88.7 dB. The coherently composing 16 complex OCT signals (4 channels × 4 B-scans, see Sec. 2.4) will provide OCT intensity image which is comparable to that of an OCT device with 94.7 dB. The axial resolution was measured to be 8.5 µm in air, which is corresponding to the axial resolution of 6.2 μm in tissue (1.38 refractive index).

2.2. Compact JM-OCT implementation

2.2.1. Compact optical module

As shown in Fig. 2, the size of the developed JM-OCT device is dramatically smaller than conventional JM-OCT devices [39,40]. The developed JM-OCT device was designed and implemented to mount all optical components on a retinal scanning unit that was developed by the Tomey Corporation, whereas the retinal scanning unit and other optical components are built separately in conventional JM-OCT devices. Because the scanning unit is motorized to translate the retinal scanning interface, an operator can easily move around the interface.

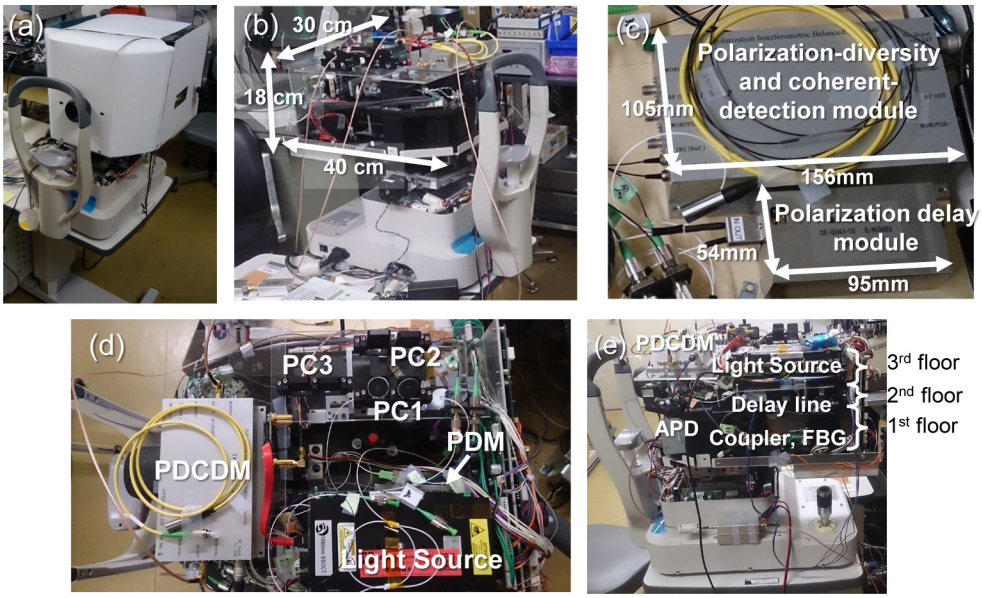

Fig. 2. Pictures of the developed JM-OCT device (a), developed JM-OCT device without cover (b), encapsulated polarization-diversity and coherent-detection module (PDCDM) and passive polarization delay module (PDM) (c), top view of the developed JM-OCT device (d), and side view of the developed JM-OCT device (e).

To make the size of the JM-OCT device compact, we employed an encapsulated PDM and PDCDM. The total volumetric size of this PDM and PDCDM was reduced to approximately one hundredth the size of the previous PDM and PDCDM [39]. This compact manufacturing is

Biomedical Optics EXPRESS

achieved by removing the mechanics for the alignment of the optical elements. The previous PDM and PDCDM consist of not only optical elements but also their alignment mechanics, and it increases the size of modules. In contrast, the new compact modules use a micro-optics integration technique, by which the optical elements are finely aligned before they are rigidly fixed onto the base plates.

2.2.2. Temperature-stable implementation

Although placing all components into a single package enabled the developed JM-OCT device to have a compact housing, this tight implementation caused another issue: temperature elevation in the package. Namely, the change in temperature around the optical fiber couplers results in probe power alteration. In detail, as shown in Fig. 1(c), the incident beam of the PDM first passes through the linear polarizer LP1. Hence, the throughput of the PDM as well as the probe power are affected by the polarization state of the incident beam. To maximize the throughput, the polarization state of the incident beam is carefully optimized by fiber polarization controller PC1 during the system building process. However, this optimization is impaired by heat-induced polarization alteration of the coupler. In the coupler, the heat expansion at the fiber bonding elevates the stress on the fibers and hence alters the polarization states.

In previously developed JM-OCT devices [39,40], this problem rarely happens because these conventional devices have sufficient space between each optical component. Moreover, the retinal scanning unit and other optical components are built separately. In contrast, the developed compact JM-OCT device was designed to pack all optical and electric components into a single chamber, as shown in Fig. 2. Therefore, once the retinal scanning unit is powered, the electrical circuit board easily heats up the chamber, and it results in the probe power instability.

To solve this problem, we replaced the conventional 99:1 and 90:10 fiber couplers with new temperature-stabilized couplers (both manufactured by Tatsuta Electric Wire & Cable Co., Ltd). This coupler uses soft glue for the fiber bonding. Hence, its expansion does not alter the pressure on the fiber so that the polarization property of the fiber is more robust to temperature changes [47].

The relationship between temperature and probe power of the developed JM-OCT device was investigated before and after replacing the 99:1 and 90:10 couplers. The probe power and temperature inside the retinal scanner were measured after the power supply for the scanner was turned on. Figure 3(a) shows the time profiles of the temperature inside the retinal scanner and the probe power of the developed JM-OCT device with the conventional and new couplers. Whereas the probe power of the JM-OCT device with the conventional fiber couplers (circles) decreases approximately linearly as temperature increases [Fig. 3(b)], the probe power of the JM-OCT device with the new temperature-stabilized fiber couplers (triangle) remains almost constant. Hence, a compact fiber-based JM-OCT device without frequent polarization state control is achieved.

2.3. Scan protocol

A 6 mm × 6 mm area around the macular region is scanned with 512 (horizontal) × 256 (vertical) sampling locations. For each vertical location, four repeated B-scans are acquired. In total, 524,288 A-lines are acquired. The time lag between successive B-scans is 6.4 ms. One volumetric scan is completed within 6.6 s.

2.4. Signal processing and image formation

The acquired spectra are processed to obtain four complex OCT signals. Here, the spectral shift correction to suppress phase fluctuation due to trigger jitter [39], re-sampling to obtain a k-linear signal [48], digital dispersion compensation [49], Fourier transform, and fixed-pattern-noise removal (median subtraction [50]) are applied. Sub-pixel axial shift correction among the

Biomedical Optics EXPRESS

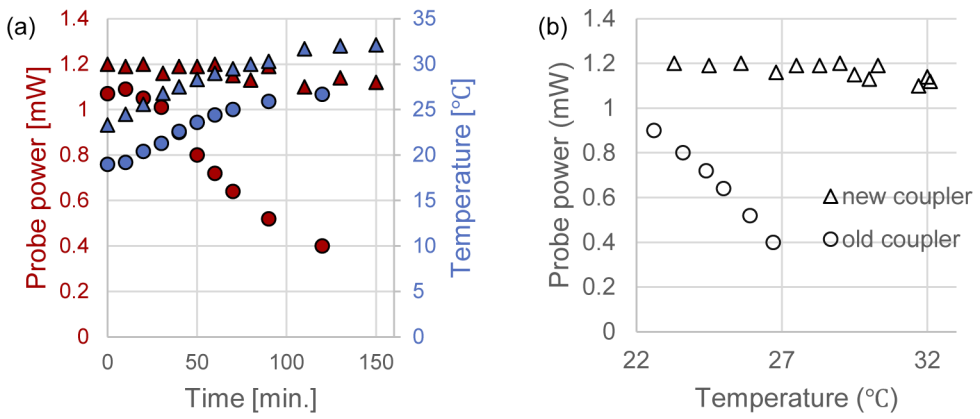

Fig. 3. Probe power stability. (a) Change in probe power with respect to temperature over time. (b) Relationship between temperature and probe power. Circles and triangles indicate data acquired using the JM-OCT device with conventional fiber couplers and the new stable couplers, respectively.

four complex OCT signals [51] is applied. This also corrects the 1st-order polarization mode dispersion.

The scattering intensity, which is similar to that of conventional OCT, is computed by coherently composing 4 polarization channels and 4 repeated B-scans [39]. The OCTA is obtained by complex correlation with noise correction [10]. The DOPU is computed using a noise correction algorithm [52]. The cross-sectional DOPU images are created using the DOPU and scattering intensity for visualization [41]. The DOPU value is used to index a color table, and the saturation of the image is determined by the intensity.

The local birefringence is estimated by combining the depth-localized Jones matrix analysis and subsequent maximum *a posteriori* (MAP) birefringence estimation [53]. Jones matrix analysis is applied with 8-pixel depth separation (27 μm in tissue with a refractive index of 1.38) and the MAP estimation was applied using four data points of the four repeated B-scans. The birefringence estimator provides a MAP estimate of the local birefringence and the reliability of the estimation.

Although we obtain multiple image functions using JM-OCT, they represent optical properties and are not tissue-specific images. Hence, some further steps are required to interpret the images. These steps become more difficult when the three-dimensional images are converted into lower-dimensional data such as projection images. Here, we provide an image to represent the RPE melanin by synthesizing attenuation, DOPU, and OCTA images according to prior knowledge of the appearance of these various images at the RPE {Eq. (1) of Ref. [44]}. We call this image an RPE-melanin image. The segmentation of RPE pixels is obtained by binarization of this RPE-melanin image [44].

Several *en face* images were created from these images. Pigment-and-flow (PAF) imaging from the OCTA and DOPU [41] show the vasculature and the abnormalities of the vasculature and RPE simultaneously. The projection of the RPE-melanin image represents the RPE pigmentation distribution. The *en face* images are created from two or three volumes. After splitting the *en face* images of each volume into sub-strips according to the large eye motion, all sub-strips were stitched using the "MosaicJ" plugin [54] of Fiji [55], as described in [41].

Biomedical Optics EXPRESS

3. Result

One healthy and several pathologic subjects were scanned using the developed JM-OCT device. Here, we demonstrate the multi-functional visualization of posterior eye tissues.

3.1. Normal healthy eye

Figure 4 shows the multi-functional images of a non-pathological subject: scattering intensity, OCTA, DOPU, RPE-melanin image, and binarized RPE-melanin image overlaid on the scattering intensity. Scattering intensity and OCTA images [Fig. 4(a) and (b)] show structure and blood flow, respectively. At the outer retina under the retinal vessels, a trailing artifact is observed in the OCTA image. Blood flow of the choriocapillaris may cause a high flow signal at the choroidal stroma to be widespread. The DOPU image [Fig. 4(c)] shows the melanin-containing tissues as low-DOPU regions. In this image, the RPE and choroidal stroma appear as low-DOPU regions.

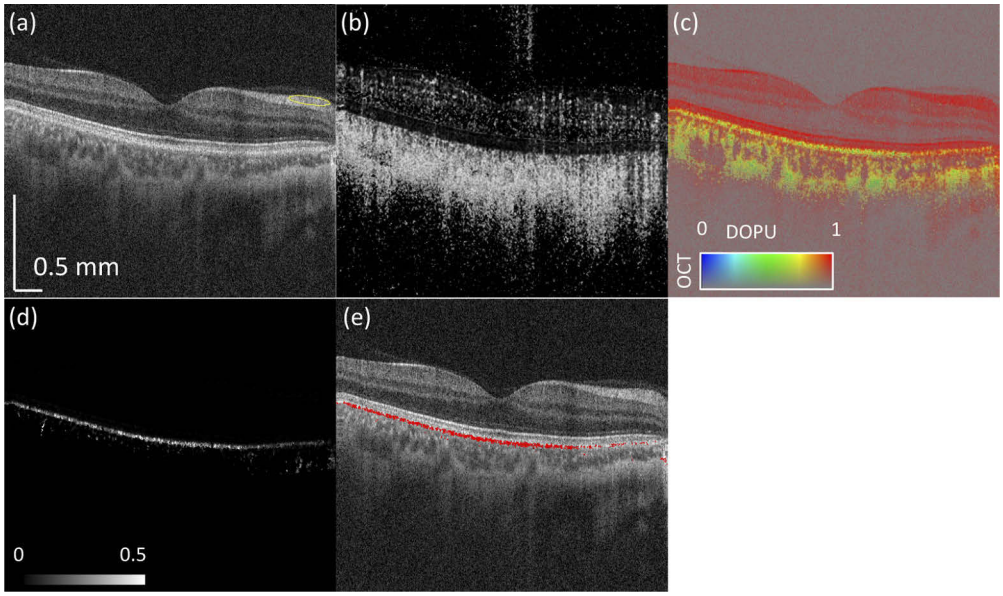

Fig. 4. Multiple images obtained by multi-functional OCT with a non-pathological case. (a) Scattering intensity, (b) OCTA, (c) DOPU, (d) RPE-melanin image, and (e) segmented RPE (red) overlaid on scattering intensity. The scale bar indicates 0.5 mm × 0.5 mm.

The local birefringence of the nerve fiber layer [yellow circle in Fig. 4(a)] is calculated. The weighted-average of the local birefringence with MAP estimation reliability inside of the yellow circle is calculated as 0.56×10^{-3}. The order of this value is in good agreement with previous PS-OCT measurements of the nerve fiber layer's birefringence [17,22,40,56–58].

The RPE-melanin image [Fig. 4(d)] has a high contrast between the RPE and non-RPE regions. The binarized RPE-melanin image overlaid on the scattering intensity image [Fig. 4(e)] selectively visualizes the RPE-melanin distribution. Near the optic nerve head (ONH) (on the left side), the DOPU at the RPE is high [Fig. 4(c)] and hence the RPE-melanin image [Fig. 4(d)] is low with respect to the fovea. As a result, the density of the segmented RPE pixels is low in this region [Fig. 4(e)]. This is probably because of the melanin density has a peak at the fovea that decreases as the ONH is approached [59]. The other possible reason is that the polarization state of incident light on the RPE at this location has been modulated by the above thick retinal nerve fiber layer. Because the DOPU value depends on the input polarization state [60], DOPU values at the fovea and close to the ONH could not be compared.

Biomedical Optics EXPRESS

3.2. Pathological cases

To evaluate prototype device, it was installed in the Tokyo Medical University Ibaraki Medical Center, and posterior pathologic cases were imaged. The present study adhered to the tenets of the Declaration of Helsinki and was approved by the Institutional Review Boards of Tokyo Medical University.

In addition to the JM-OCT images, we also obtained several images of clinical modalities such as color fundus photography and fundus autofluorescence imaging. The near-infrared autofluorescence (NIR-AF) images were recorded with a confocal scanning laser ophthalmoscope (HRA 2, Heidelberg Engineering, Germany) having an excitation wavelength of 788 nm and detected emission wavelength greater than 800 nm. The high intensity in NIR-AF is thought to represent melanin distribution [61].

3.2.1. Case of fibrosis

Figure 5 shows an AMD subject with subretinal fibrosis. The subretinal fibrosis structure appears as a white region in the color fundus photograph [Fig. 5(a)]. The *en face* PAF image [Fig. 5(d)] and RPE-melanin image [Fig. 5(c)] show that there is a wide area of low pigmentation and abnormal vascularization (blue ovals). The PAF image exhibits a yellow color in this region because the abnormal blood flow signal is located above the pigmented tissues. The high RPE-melanin image regions agree well with the hyper auto-fluorescence in the NIR-AF image [Fig. 5(b)] (green arrows). A cross-sectional image of the scattering intensity [Fig. 5(e)] shows the subretinal fibrosis structure as a hyperreflective region. The DOPU cross-sectional image [Fig. 5(g)] shows that RPE melanin and choroidal stromal melanin are distributed separately. The RPE-melanin and segmented RPE overlaid on the intensity images [Fig. 5(h) and (i)] selectively visualizes the irregular distribution of RPE melanin. In the PAF image, there are some pink regions, as indicated by the white arrow in Fig. 5(d). In these regions, the DOPU value at the elevated RPE is slightly smaller than unity, and there is a substantial blood flow signal immediately under the RPE [white circles in Fig. 5(g) and (f)]. The broad bright yellow region in the PAF image [blue circle in Fig. 5] also exhibits a DOPU value slightly below unity, however, there is indication of blood flow around or above the melanin layer (the cross sectional images are not shown). These appearances may indicate defects of the RPE. In contrast, the bright yellow to white regions [black arrows in Fig. 5] show the almost unity DOPU values at the RPE.

3.2.2. Case of retinal hemorrhage

Figure 6 shows a subretinal hemorrhage case. The color fundus image [Fig. 6(a)] shows a dark red hemorrhage region between the optic nerve head and macula, where the dashed line indicates the location of cross-sectional images [Fig. 6(e)–(j)]. As shown in the scattering intensity and DOPU [Fig. 6(e) and (g)], there is an RPE elevation at the location of the hemorrhage. Above the elevated RPE, there is a hyperreflective region [white arrow in Fig. 6(e)]. The hyper appearance of the RPE-melanin image coincides with the moderately high auto-fluorescence pattern in the NIR-AF [green arrows in Figs. 6(b) and (c)].

3.2.3. Cases of choroidal neovascularization

Figure 7 shows a choroidal neovascularization (CNV) subject. The scattering intensity image [Fig. 7(e)] shows hyper-transmission beneath the RPE-Bruch's membrane band in the center of the fovea, which suggests the absence of RPE (white arrow). In the OCTA image [Fig. 7(f)], the presence of CNV is shown above the hyper-transmission (green arrow). Moreover, the DOPU [Fig. 7(g)] shows the RPE defect and thickened RPE surrounding the CNV region (black arrow). The donut pattern corresponding to this thickened RPE is clearly visible in the RPE-melanin projection, and it corresponds well with the NIR-AF image [blue arrows in Figs. 7(b) and (c)].

Biomedical Optics EXPRESS

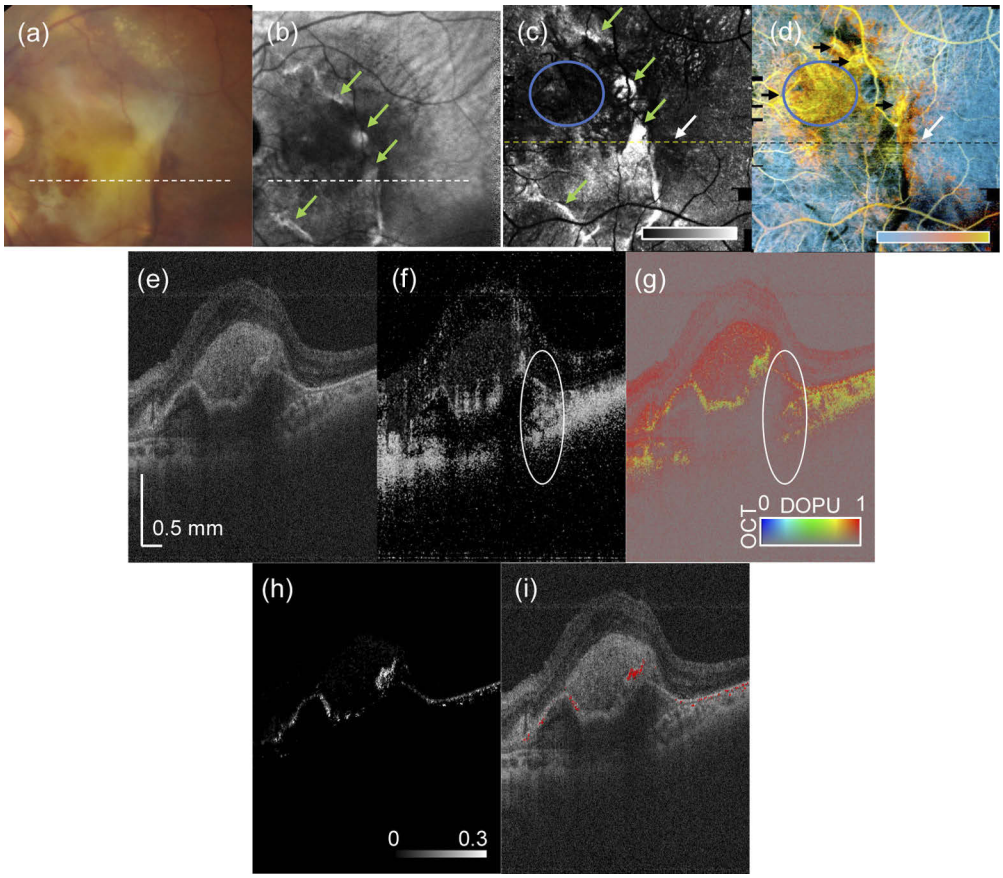

Fig. 5. Multiple images obtained by multi-functional OCT and segmentation results for a case with fibrosis. A color fundus photograph (a) and NIR-AF (b) were obtained. The *en face* maps of (c) RPE-melanin and (d) PAF images and the cross sections of (e) scattering intensity, (f) OCTA, (g) DOPU, (h) RPE-melanin, and (i) RPE (red) overlaid on scattering intensity images at the dotted lines in *en face* maps are shown. The scale bar indicates 0.5 mm × 0.5 mm.

Figure 8 shows an AMD subject with CNV and hard exudates. The color fundus photograph [Fig. 8(a)] shows that there are hard exudates in the inferior region (whitish orange, indicated by a green circle), which appears as hypo-autofluorescence in the NIR-AF [green circle in Fig. 8(b)]. In the scattering intensity [Fig. 8(e)], hyperreflective materials are shown in both the subretinal and intraretinal regions (white arrows). In the DOPU image [Fig. 8(g)], the corresponding region shows a low DOPU appearance (white arrows). Because a previous study reported that hard exudates appear as low DOPU [25], we suspect that this hyperreflective material can be considered to be hard exudates. At the fovea, abnormal blood flow signals appear in the OCTA [white circle in Fig. 8(l)]. And there are low DOPU region surrounding the CNV [orange arrows in Fig. 8(c) and (m)]. This is maybe thickened RPE as same as shown in the CNV case [Fig. 7(c) and (g)], however, NIF-AF shows hypo-autofluorescence at the fovea [Fig. 8(b)]. In the OCT cross section, there is high scattering materials under the retina at the fovea [blue arrow in Fig. 8(k)].

Biomedical Optics EXPRESS

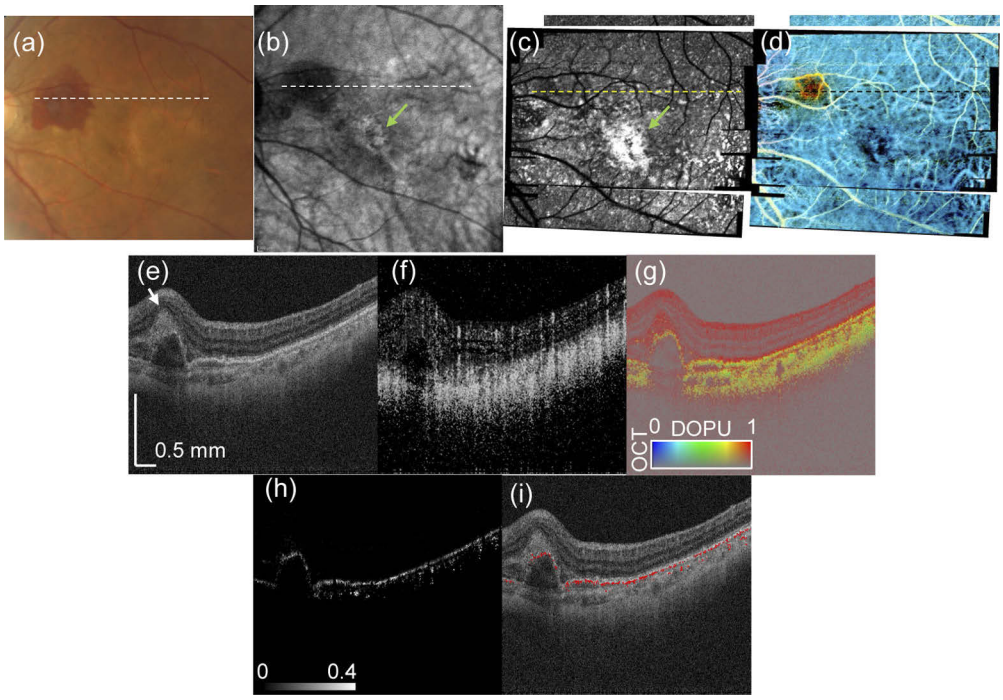

Fig. 6. Multiple images obtained by multi-functional OCT and segmentation results for a subretinal hemorrhage case. A color fundus photograph (a) and NIR-AF (b) were obtained. The *en face* maps of (c) RPE-melanin and (d) PAF images and the cross sections of (e) scattering intensity, (f) OCTA, (g) DOPU, (h) RPE-melanin, and (i) RPE (red) overlaid on scattering intensity images at the dotted lines in *en face* maps are shown. The scale bar indicates 0.5 mm × 0.5 mm.

3.2.4. Subretinal hyperreflective material of AMD

Figure 9 shows the results for five AMD subjects. Three cases (upper row) show subretinal fibrosis [Fig. 9(a)–(c)], while the other cases (lower row) show subretinal hemorrhage [Fig. 9(d) and (e)]. All subjects show hyperreflective material in the OCT, which were recently referred to as subretinal hyperreflective material (SHRM) [62,63]. The quantitative nature of the birefringence measurement enables the quantitative comparison of SHRM birefringence. The local birefringence values of SHRM [yellow circle in Fig. 9(a)–(e)] are calculated by weighted average with the MAP estimation reliability. The pixels that exhibit low DOPU values (< 0.9) are excluded from the calculation to avoid unreliable local birefringence estimates. The mean value of estimated local birefringence in the yellow circle regions of interest are 2.09×10^{-3}, 1.96×10^{-3}, and 1.96×10^{-3} in the fibrosis cases and 1.28×10^{-3} and 1.22×10^{-3} in the hemorrhage cases. Hence, we quantitatively conclude that the birefringence of the SHRM in the fibrosis case is larger than that in the hemorrhage case.

Biomedical Optics EXPRESS

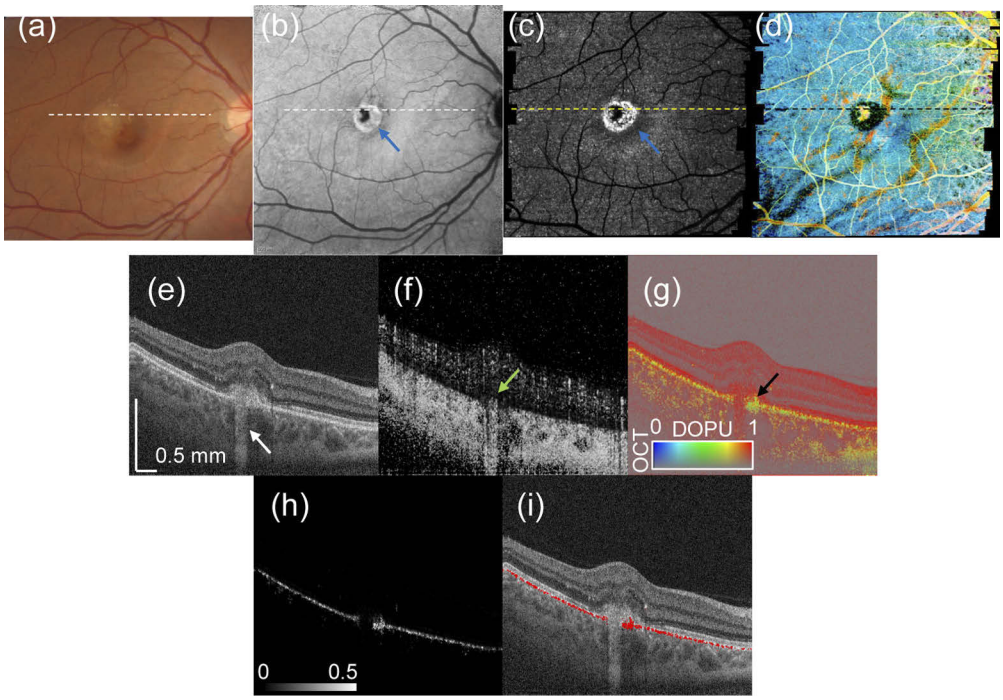

Fig. 7. Multiple images obtained by multi-functional OCT and segmentation results for a CNV case. A color fundus photograph (a) and NIR-AF (b) were obtained. The *en face* maps of (c) RPE-melanin and (d) PAF images and the cross sections of (e) scattering intensity, (f) OCTA, (g) DOPU, (h) RPE-melanin, and (i) RPE (red) overlaid on scattering intensity images at the dotted lines in *en face* maps are shown. The scale bar indicates 0.5 mm × 0.5 mm.

Biomedical Optics EXPRESS

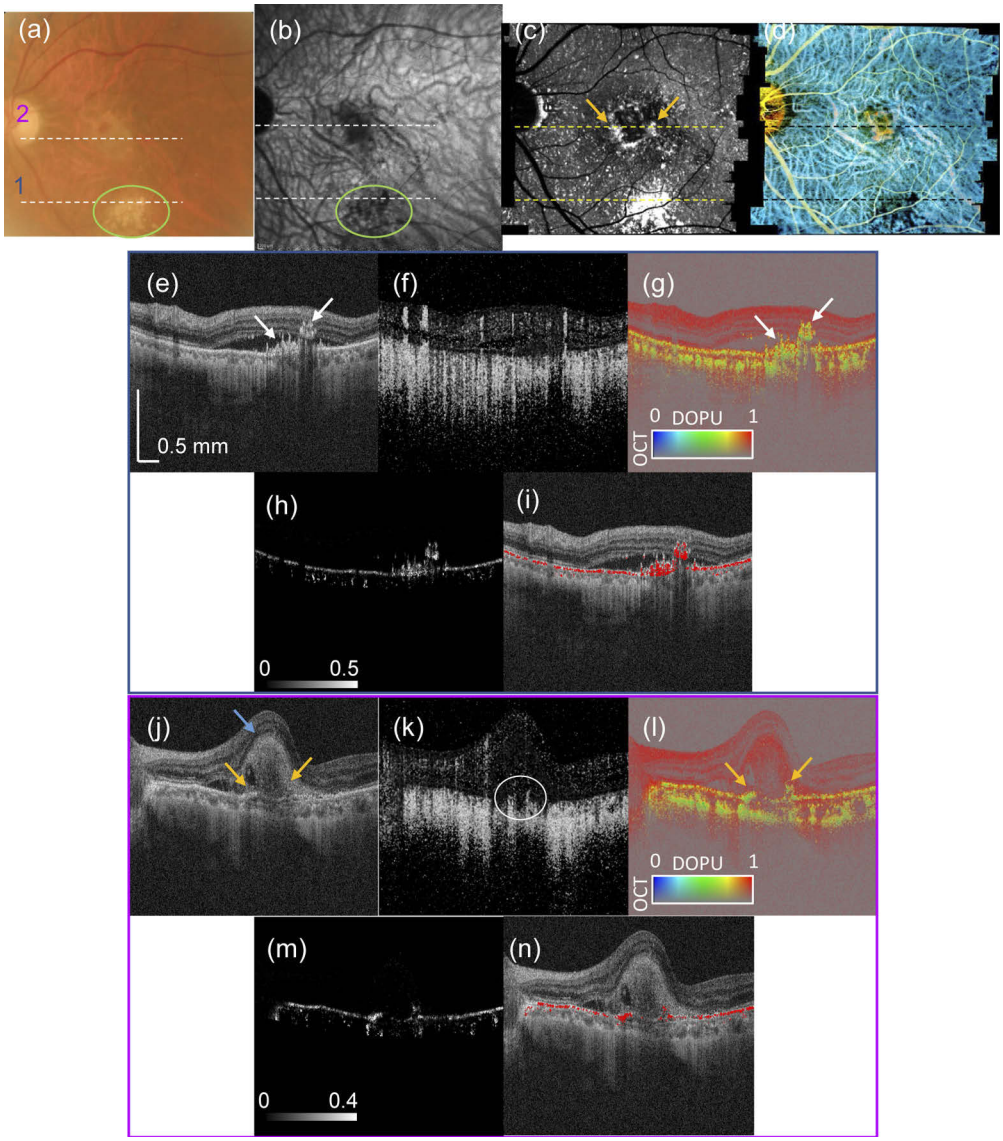

Fig. 8. Multiple images obtained by the multi-functional OCT and segmentation results for a CNV case. A color fundus photograph (a) and NIR-AF (b) were obtained. The *en face* map of (c) RPE-melanin and (d) PAF image and the cross sections of (e, j) scattering intensity, (f, k) OCTA, (g, l) DOPU, (h, m) RPE-melanin, and (i, n) RPE (red) overlaid on scattering intensity images at the dotted lines (1: e–i, 2: j–n) in *en face* maps are shown. The scale bar indicates 0.5 mm × 0.5 mm.

Biomedical Optics EXPRESS

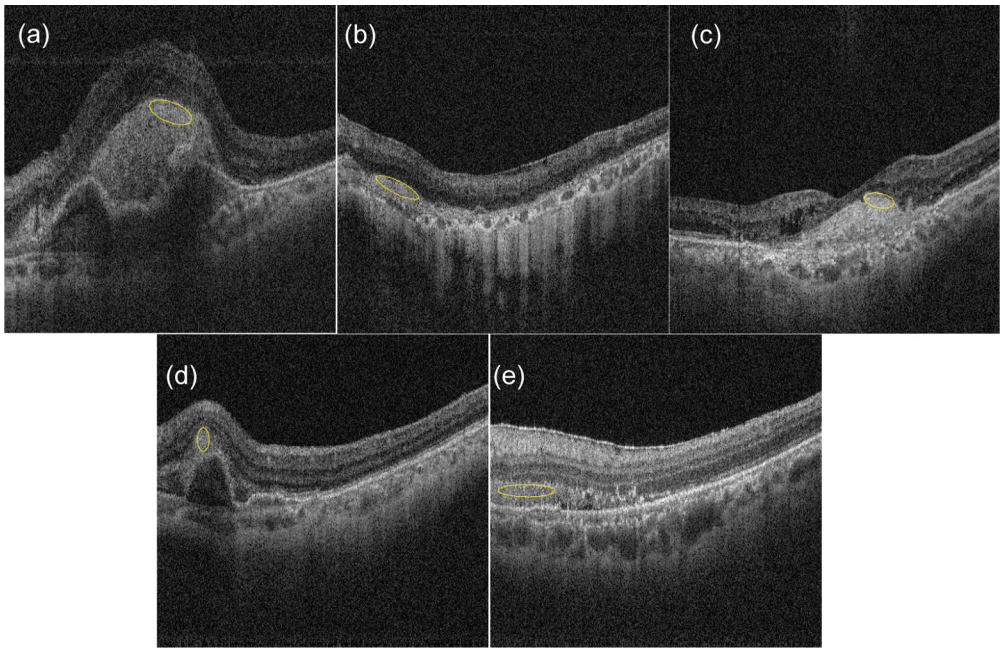

Fig. 9. Several cases with subretinal hyperreflective material. OCT intensity images in (a, b, c) fibrosis cases and (d, e) hemorrhage cases. The local birefringence values are measured in the yellow circles.

Biomedical Optics EXPRESS

4. Discussion

4.1. DOPU vs RPE-melanin image

The content of melanin in tissue is one of sources causing the randomness of the polarization state of backscattered light [64]. Hence, a DOPU image was used to visualize the abnormality of the RPE, which is melanin-rich tissue [27,43,65,66]. However, DOPU also exhibits melanin in the choroid [42,67]. Hence, tissue discrimination is required to correctly map the RPE integrity [43,66]. In this paper, we introduced the RPE-melanin imaging by combining multiple image functions.

To demonstrate the power of the RPE-melanin image, we compared three types of *en face* images. The first one is an *en face* projection of the DOPU, the second is an *en face* projection of RPE-melanin image, and the third is NIR-AF, which is one of the standard methods for assessing RPE abnormality. The *en face* RPE-melanin images are created by summing the values along depth. Figure 10 shows the obtained *en face* images of two subjects. The *en face* projections of the RPE-melanin image visualize specific patterns of signature of abnormalities and which agrees well with the hyper-autofluorescence patterns of NIR-AF images in both the CNV and subretinal fibrosis subjects. However, some specific patterns are not visible in the case of the *en face* projection of the DOPU [green circles in Fig. 10(a, c, e) and green arrows in Fig. 10(b, d, f)]. Because the RPE-melanin image suppresses the contribution from choroidal stromal melanin, the RPE-melanin images enhance the contrast of RPE melanin. The *en face* map of RPE-melanin image offers suitable imaging for the qualitative assessment of RPE melanin.

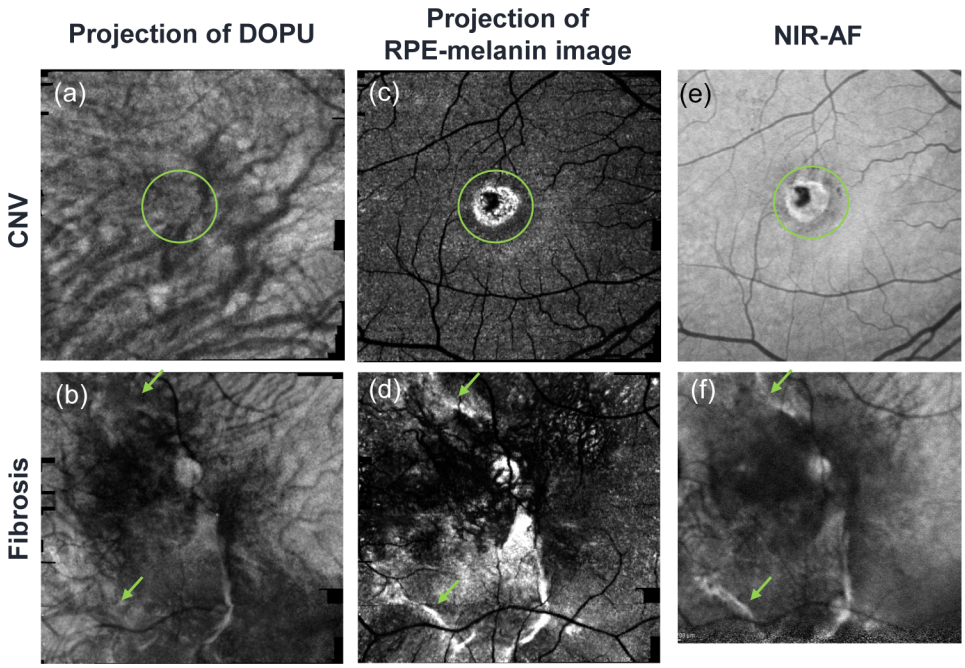

Fig. 10. *En face* projections of (a, b) DOPU and (c, d) RPE-melanin image, and (e, f) NIR-AF of (a, c, e) CNV and (b, d, f) fibrosis subjects. Some abnormal signatures are not appeared in DOPU projection (green circle and arrow), while high melanin signal patterns in RPE-melanin image are in good agreement with hyper-autofluorescence pattern of NIR-AF.

Biomedical Optics EXPRESS

4.2. Comparison of system specifications with those of other clinical JM-OCT devices

The presented clinical prototype JM-OCT uses the same specifications of the light source and digitizer to those of previous prototypes [40,41]. Hence, the basic performance of OCT imaging, such as resolution and sensitivity, are similar, as shown in Table 1.

Table 1. Comparison of the specifications of the proposed device with those of the posterior eye JM-OCT devices developed by Sugiyama *et al.* [40] and Makita *et al.* [41].

		Presented device	Clinical test type [40]	Simplified device [41]
Probe power	[mW]	1.4	1.4	1.0
Sensitivity[1]	[dB]	88.7	91.6	89.5
Sensitivity roll-off	[dB/mm]	−0.63	−0.63	−0.75
Resolution (axial, in air)	[μm]	8.5	8.9	8.3
Available function		Intensity, OCTA, DOPU, phase retardation	Intensity, OCTA, DOPU, phase retardation	Intensity, OCTA, DOPU
Data size[2]	[GB]	5	5	2.5
Imaging range (axial, in tissue)	[mm]	2.2	2.2	2.7
Footprint	[cm]	40 × 30	100 × 30	54.5 × 53.5

[1]Average of all polarization channels
[2]512 × 256 × 4 A-lines

The previous JM-OCT prototype requires an additional module box to package the bulk optics of the PDM and PDCDM parts [40]. Hence, the footprint is still large compared with commercial OCT devices. It also requires an optic fiber to connect the optical module and a retinal scanning head. Hence, the polarization state of the probe beam alters when the scanning head moves. The compact package size and light load of data acquisition and processing are obtained by discarding the ability to measure phase retardation [41]. The prototype presented in this paper achieves both a compact size and the full functionality of JM-OCT.

4.3. Computational time

One disadvantage of multi-functional imaging by JM-OCT is its long computational time. This slow speed is mainly caused by the MAP estimation in the birefringence image computation. In the original demonstration of a MAP estimator for birefringence estimation processed by a Windows 10 PC with Intel Core i7-4910MQ CPU and 16 GB RAM, it takes 31 s with four frames of repeatable B-scans [53]. If the volumetric scan consists of 256 B-scans, the birefringence estimation would take approximately 132 minutes.

To accelerate the computation of multi-functional OCT images, the developed JM-OCT system exploits GPU processing for image formation. The processing time of local birefringence estimation was reduced to approximately 1 s with four-frame repetition on a Windows 10 PC (Intel Core i9-7900X CPU and 128 GB RAM, NVidia GeForce GTX 1080 Ti). The total time needed to process the sensitivity-enhanced scattering, OCTA, DOPU, and MAP of local birefringence is approximately 12 minutes. The tissue-specific image synthesis and *en face* PAF imaging take 1 minute each.

Biomedical Optics EXPRESS

4.4. Multi-functional imaging of subretinal hyperreflective material and hyperreflective foci

SHRM is a biomarker of AMD treatment with anti-vascular endothelial growth factor drugs [68]. SHRM may contain different types of tissue such as exudates, blood, neovascularization, and fibrin. Because all these types of tissues are similarly hyperreflective, it is difficult to differentiate them using only conventional scattering-based OCT.

Multi-functional OCT imaging might be useful for the sub-type classification of SHRM. For example, it was reported that OCTA is useful for discriminating vascular and avascular SHRM [69,70]. In addition, as we have shown in Section 3.2.4, the SHRM of fibrosis and hemorrhages show different birefringence properties. The JM-OCT may better discriminate SHRM subtypes than standard OCT.

In addition to the SHRM, the presence of hyperreflective foci in the intraretinal layer is also considered to be a candidate AMD biomarker [71–73]. Several mechanisms are expected to be the origin of the hyperreflective foci, such as lipofuscin aggregation and RPE migration [72], and hence it is natural to think that hyperreflective foci may also have some subtypes. Among several modalities, DOPU imaging with polarization-sensitive OCT has shown the potential to discriminate hyperreflective foci originating from RPE melanin [27,74]. Similarly, JM-OCT might have the ability to discriminate RPE-originated hyperreflective foci.

These abilities of JM-OCT indicate that it is a promising diagnostic tool for AMD.

5. Conclusion

A clinical-grade multi-functional OCT device based on JM-OCT has been developed. The *in vivo* posterior eye imaging of AMD subjects suggests that this method enables the differentiation of abnormal tissues. We believe that posterior eye imaging using the developed system will advance the investigation of eye diseases and exploration of clinical applications of multi-functional OCT in ophthalmology.

Funding

Japan Society for the Promotion of Science (15K13371); Japan Science and Technology Agency (JPMJMI18G8); Program for building Regional Innovation Ecosystems of Ministry of Education, Culture, Sports, Science and Technology.

Acknowledgment

The technical assistance from Tomey Corporation and support for patient measurement from co-medical staffs of Tokyo Medical University Ibaraki Medical Center are gratefully acknowledged. Shinnosuke Azuma is currently employed by Topcon Inc. Deepa Kasaragod is currently employed at Graduate School of Biomedical and Health Sciences, Hiroshima University. We also acknowledge the research administrative work of Tomomi Nagasaka from the University of Tsukuba.

Disclosures

SA, DK: Tomey Corp. (F), TOPCON (F), Nidek (F), Kao (F); SM, YY; Tomey Corp. (F, P), TOPCON (F), Nidek (F), Kao (F); SS: Tomey Corp. (E); MM Allergan (F), Alcon (F), Novartis (F,R), Santen (F,R), Bayer (F).

References

1. D. Huang, E. A. Swanson, C. P. Lin, J. S. Schuman, W. G. Stinson, W. Chang, M. R. Hee, T. Flotte, K. Gregory, C. A. Puliafito, and J. G. Fujimoto, "Optical coherence tomography," Science **254**(5035), 1178–1181 (1991).

Biomedical Optics EXPRESS

2. S. Makita, Y. Hong, M. Yamanari, T. Yatagai, and Y. Yasuno, "Optical coherence angiography," Opt. Express **14**(17), 7821–7840 (2006).
3. J. Fingler, R. J. Zawadzki, J. S. Werner, D. Schwartz, and S. E. Fraser, "Volumetric microvascular imaging of human retina using optical coherence tomography with a novel motion contrast technique," Opt. Express **17**(24), 22190–22200 (2009).
4. D. Y. Kim, J. Fingler, J. S. Werner, D. M. Schwartz, S. E. Fraser, and R. J. Zawadzki, "*In vivo* volumetric imaging of human retinal circulation with phase-variance optical coherence tomography," Biomed. Opt. Express **2**(6), 1504–1513 (2011).
5. G. Liu, L. Chou, W. Jia, W. Qi, B. Choi, and Z. Chen, "Intensity-based modified Doppler variance algorithm: Application to phase instable and phase stable optical coherence tomography systems," Opt. Express **19**(12), 11429–11440 (2011).
6. Y. Jia, O. Tan, J. Tokayer, B. Potsaid, Y. Wang, J. J. Liu, M. F. Kraus, H. Subhash, J. G. Fujimoto, J. Hornegger, and D. Huang, "Split-spectrum amplitude-decorrelation angiography with optical coherence tomography," Opt. Express **20**(4), 4710–4725 (2012).
7. J. Enfield, E. Jonathan, and M. Leahy, "*In vivo* imaging of the microcirculation of the volar forearm using correlation mapping optical coherence tomography (cmOCT)," Biomed. Opt. Express **2**(5), 1184–1193 (2011).
8. R. K. Wang, S. L. Jacques, Z. Ma, S. Hurst, S. R. Hanson, and A. Gruber, "Three dimensional optical angiography," Opt. Express **15**(7), 4083–4097 (2007).
9. A. S. Nam, I. Chico-Calero, and B. J. Vakoc, "Complex differential variance algorithm for optical coherence tomography angiography," Biomed. Opt. Express **5**(11), 3822–3832 (2014).
10. S. Makita, K. Kurokawa, Y.-J. Hong, M. Miura, and Y. Yasuno, "Noise-immune complex correlation for optical coherence angiography based on standard and Jones matrix optical coherence tomography," Biomed. Opt. Express **7**(4), 1525–1548 (2016).
11. Y. Jia, S. T. Bailey, D. J. Wilson, O. Tan, M. L. Klein, C. J. Flaxel, B. Potsaid, J. J. Liu, C. D. Lu, M. F. Kraus, J. G. Fujimoto, and D. Huang, "Quantitative optical coherence tomography angiography of choroidal neovascularization in age-related macular degeneration," Ophthalmology **121**(7), 1435–1444 (2014).
12. T. S. Hwang, Y. Jia, S. S. Gao, S. T. Bailey, A. K. Lauer, C. J. Flaxel, D. J. Wilson, and D. Huang, "Optical coherence tomography angiography features of diabetic retinopathy:," Retina **35**(11), 2371–2376 (2015).
13. M. Miura, Y.-J. Hong, Y. Yasuno, D. Muramatsu, T. Iwasaki, and H. Goto, "Three-dimensional vascular imaging of proliferative diabetic retinopathy by Doppler optical coherence tomography," Am. J. Ophthalmol. **159**(3), 528–538.e3 (2015).
14. Y. Jia, E. Wei, X. Wang, X. Zhang, J. C. Morrison, M. Parikh, L. H. Lombardi, D. M. Gattey, R. L. Armour, B. Edmunds, M. F. Kraus, J. G. Fujimoto, and D. Huang, "Optical coherence tomography angiography of optic disc perfusion in glaucoma," Ophthalmology **121**(7), 1322–1332 (2014).
15. J. F. de Boer, T. E. Milner, and J. S. Nelson, "Determination of the depth-resolved Stokes parameters of light backscattered from turbid media by use of polarization-sensitive optical coherence tomography," Opt. Lett. **24**(5), 300–302 (1999).
16. C. Hitzenberger, E. Götzinger, M. Sticker, M. Pircher, and A. Fercher, "Measurement and imaging of birefringence and optic axis orientation by phase resolved polarization sensitive optical coherence tomography," Opt. Express **9**(13), 780–790 (2001).
17. E. Götzinger, M. Pircher, B. Baumann, C. Hirn, C. Vass, and C. K. Hitzenberger, "Retinal nerve fiber layer birefringence evaluated with polarization sensitive spectral domain OCT and scanning laser polarimetry: A comparison," J. Biophotonics **1**(2), 129–139 (2008).
18. Y. Yasuno, M. Yamanari, K. Kawana, T. Oshika, and M. Miura, "Investigation of post-glaucoma-surgery structures by three-dimensional and polarization sensitive anterior eye segment optical coherence tomography," Opt. Express **17**(5), 3980–3996 (2009).
19. S. Fukuda, S. Beheregaray, D. Kasaragod, S. Hoshi, G. Kishino, K. Ishii, Y. Yasuno, and T. Oshika, "Noninvasive evaluation of phase retardation in blebs after glaucoma surgery using anterior segment polarization-sensitive optical coherence tomography," Invest. Ophthalmol. Visual Sci. **55**(8), 5200–5206 (2014).
20. M. Yamanari, S. Tsuda, T. Kokubun, Y. Shiga, K. Omodaka, Y. Yokoyama, N. Himori, M. Ryu, S. Kunimatsu-Sanuki, H. Takahashi, K. Maruyama, H. Kunikata, and T. Nakazawa, "Fiber-based polarization-sensitive OCT for birefringence imaging of the anterior eye segment," Biomed. Opt. Express **6**(2), 369–389 (2015).
21. F. Beer, A. Wartak, N. Pircher, S. Holzer, J. Lammer, G. Schmidinger, B. Baumann, M. Pircher, and C. K. Hitzenberger, "Mapping of corneal layer thicknesses with polarization-sensitive optical coherence tomography using a conical scan pattern," Invest. Ophthalmol. Visual Sci. **59**(13), 5579–5588 (2018).
22. B. Cense, T. C. Chen, B. H. Park, M. C. Pierce, and J. F. de Boer, "Thickness and birefringence of healthy retinal nerve fiber layer tissue measured with polarization-sensitive optical coherence tomography," Invest. Ophthalmol. Visual Sci. **45**(8), 2606–2612 (2004).
23. M. Pircher, E. Götzinger, O. Findl, S. Michels, W. Geitzenauer, C. Leydolt, U. Schmidt-Erfurth, and C. K. Hitzenberger, "Human macula investigated *in vivo* with polarization-sensitive optical coherence tomography," Invest. Ophthalmol. Visual Sci. **47**(12), 5487–5494 (2006).
24. M. Miura, M. Yamanari, T. Iwasaki, A. E. Elsner, S. Makita, T. Yatagai, and Y. Yasuno, "Imaging polarimetry in age-related macular degeneration," Invest. Ophthalmol. Visual Sci. **49**(6), 2661–2667 (2008).

Biomedical Optics EXPRESS

25. Y.-J. Hong, M. Miura, M. J. Ju, S. Makita, T. Iwasaki, and Y. Yasuno, "Simultaneous investigation of vascular and retinal pigment epithelial pathologies of exudative macular diseases by multifunctional optical coherence tomography," Invest. Ophthalmol. Visual Sci. **55**(8), 5016–5031 (2014).
26. P. Roberts, M. Sugita, G. Deák, B. Baumann, S. Zotter, M. Pircher, S. Sacu, C. K. Hitzenberger, and U. Schmidt-Erfurth, "Automated identification and quantification of subretinal fibrosis in neovascular age-related macular degeneration using polarization-sensitive OCT," Invest. Ophthalmol. Visual Sci. **57**(4), 1699–1705 (2016).
27. M. Miura, S. Makita, S. Sugiyama, Y.-J. Hong, Y. Yasuno, A. E. Elsner, S. Tamiya, R. Tsukahara, T. Iwasaki, and H. Goto, "Evaluation of intraretinal migration of retinal pigment epithelial cells in age-related macular degeneration using polarimetric imaging," Sci. Rep. **7**(1), 3150 (2017).
28. S. Jiao and L. V. Wang, "Jones-matrix imaging of biological tissues with quadruple-channel optical coherence tomography," J. Biomed. Opt. **7**(3), 350–358 (2002).
29. B. H. Park, M. C. Pierce, B. Cense, and J. F. de Boer, "Jones matrix analysis for a polarization-sensitive optical coherence tomography system using fiber-optic components," Opt. Lett. **29**(21), 2512–2514 (2004).
30. S. Makita, M. Yamanari, and Y. Yasuno, "Generalized Jones matrix optical coherence tomography: Performance and local birefringence imaging," Opt. Express **18**(2), 854–876 (2010).
31. C. Fan and G. Yao, "Mapping local optical axis in birefringent samples using polarization-sensitive optical coherence tomography," J. Biomed. Opt. **17**(11), 110501 (2012).
32. M. Villiger, D. Lorenser, R. A. McLaughlin, B. C. Quirk, R. W. Kirk, B. E. Bouma, and D. D. Sampson, "Deep tissue volume imaging of birefringence through fibre-optic needle probes for the delineation of breast tumour," Sci. Rep. **6**(1), 28771 (2016).
33. N. Lippok, M. Villiger, and B. E. Bouma, "Degree of polarization (uniformity) and depolarization index: Unambiguous depolarization contrast for optical coherence tomography," Opt. Lett. **40**(17), 3954–3957 (2015).
34. M. Villiger, B. Braaf, N. Lippok, K. Otsuka, S. K. Nadkarni, and B. E. Bouma, "Optic axis mapping with catheter-based polarization-sensitive optical coherence tomography," Optica **5**(10), 1329–1337 (2018).
35. Q. Li, K. Karnowski, P. B. Noble, A. Cairncross, A. James, M. Villiger, and D. D. Sampson, "Robust reconstruction of local optic axis orientation with fiber-based polarization-sensitive optical coherence tomography," Biomed. Opt. Express **9**(11), 5437–5455 (2018).
36. M. Yamanari, S. Tsuda, T. Kokubun, Y. Shiga, K. Omodaka, N. Aizawa, Y. Yokoyama, N. Himori, S. Kunimatsu-Sanuki, K. Maruyama, H. Kunikata, and T. Nakazawa, "Estimation of Jones matrix, birefringence and entropy using Cloude-Pottier decomposition in polarization-sensitive optical coherence tomography," Biomed. Opt. Express **7**(9), 3551–3573 (2016).
37. Y. Lim, Y.-J. Hong, L. Duan, M. Yamanari, and Y. Yasuno, "Passive component based multifunctional Jones matrix swept source optical coherence tomography for Doppler and polarization imaging," Opt. Lett. **37**(11), 1958–1960 (2012).
38. B. Baumann, W. Choi, B. Potsaid, D. Huang, J. S. Duker, and J. G. Fujimoto, "Swept source / Fourier domain polarization sensitive optical coherence tomography with a passive polarization delay unit," Opt. Express **20**(9), 10229–10241 (2012).
39. M. J. Ju, Y.-J. Hong, S. Makita, Y. Lim, K. Kurokawa, L. Duan, M. Miura, S. Tang, and Y. Yasuno, "Advanced multi-contrast Jones matrix optical coherence tomography for Doppler and polarization sensitive imaging," Opt. Express **21**(16), 19412–19436 (2013).
40. S. Sugiyama, Y.-J. Hong, D. Kasaragod, S. Makita, S. Uematsu, Y. Ikuno, M. Miura, and Y. Yasuno, "Birefringence imaging of posterior eye by multi-functional Jones matrix optical coherence tomography," Biomed. Opt. Express **6**(12), 4951–4974 (2015).
41. S. Makita, T. Mino, T. Yamaguchi, M. Miura, S. Azuma, and Y. Yasuno, "Clinical prototype of pigment and flow imaging optical coherence tomography for posterior eye investigation," Biomed. Opt. Express **9**(9), 4372–4389 (2018).
42. M. Miura, S. Makita, Y. Yasuno, R. Tsukahara, Y. Usui, N. A. Rao, Y. Ikuno, S. Uematsu, T. Agawa, T. Iwasaki, and H. Goto, "Polarization-sensitive optical coherence tomographic documentation of choroidal melanin loss in chronic Vogt–Koyanagi–Harada disease," Invest. Ophthalmol. Visual Sci. **58**(11), 4467–4476 (2017).
43. M. Miura, S. Makita, S. Azuma, Y. Yasuno, S. Ueda, S. Sugiyama, T. Mino, T. Yamaguchi, H. S. Sandhu, H. J. Kaplan, T. Iwasaki, and H. Goto, "Evaluation of focal damage in the retinal pigment epithelium layer in serous retinal pigment epithelium detachment," Sci. Rep. **9**(1), 3278 (2019).
44. S. Azuma, S. Makita, A. Miyazawa, Y. Ikuno, M. Miura, and Y. Yasuno, "Pixel-wise segmentation of severely pathologic retinal pigment epithelium and choroidal stroma using multi-contrast Jones matrix optical coherence tomography," Biomed. Opt. Express **9**(7), 2955–2973 (2018).
45. B. Braaf, K. A. Vermeer, M. de Groot, K. V. Vienola, and J. F. de Boer, "Fiber-based polarization-sensitive OCT of the human retina with correction of system polarization distortions," Biomed. Opt. Express **5**(8), 2736–2758 (2014).
46. American National Standards Institute and Laser Institute of America, *American National Standard for Safe Use of Lasers* (Laser Institute of America, Orlando, FL, 2014).
47. M. Takaya, "Optical fiber coupler," PCT Patent WO2018225554 (A1), Tatsuta Electric Wire & Cable Co Ltd (2018).
48. S. Makita, T. Fabritius, and Y. Yasuno, "Full-range, high-speed, high-resolution 1-μm spectral-domain optical coherence tomography using BM-scan for volumetric imaging of the human posterior eye," Opt. Express **16**(12), 8406–8420 (2008).

Biomedical Optics EXPRESS

49. Y. Yasuno, Y. Hong, S. Makita, M. Yamanari, M. Akiba, M. Miura, and T. Yatagai, "*In Vivo* high-contrast imaging of deep posterior eye by 1-μm swept source optical coherence tomography and scattering optical coherence angiography," Opt. Express **15**(10), 6121–6139 (2007).
50. S. Moon, S.-W. Lee, and Z. Chen, "Reference spectrum extraction and fixed-pattern noise removal in optical coherence tomography," Opt. Express **18**(24), 24395–24404 (2010).
51. E. Li, S. Makita, Y.-J. Hong, D. Kasaragod, and Y. Yasuno, "Three-dimensional multi-contrast imaging of *in vivo* human skin by Jones matrix optical coherence tomography," Biomed. Opt. Express **8**(3), 1290–1305 (2017).
52. S. Makita, Y.-J. Hong, M. Miura, and Y. Yasuno, "Degree of polarization uniformity with high noise immunity using polarization-sensitive optical coherence tomography," Opt. Lett. **39**(24), 6783–6786 (2014).
53. D. Kasaragod, S. Makita, Y.-J. Hong, and Y. Yasuno, "Noise stochastic corrected maximum a posteriori estimator for birefringence imaging using polarization-sensitive optical coherence tomography," Biomed. Opt. Express **8**(2), 653–669 (2017).
54. P. Thévenaz and M. Unser, "User-friendly semiautomated assembly of accurate image mosaics in microscopy," Microsc. Res. Tech. **70**(2), 135–146 (2007).
55. J. Schindelin, I. Arganda-Carreras, E. Frise, V. Kaynig, M. Longair, T. Pietzsch, S. Preibisch, C. Rueden, S. Saalfeld, B. Schmid, J.-Y. Tinevez, D. J. White, V. Hartenstein, K. Eliceiri, P. Tomancak, and A. Cardona, "Fiji: An open-source platform for biological-image analysis," Nat. Methods **9**(7), 676–682 (2012).
56. B. Cense, T. C. Chen, B. H. Park, M. C. Pierce, and J. F. de Boer, "*In Vivo* depth-resolved birefringence measurements of the human retinal nerve fiber layer by polarization-sensitive optical coherence tomography," Opt. Lett. **27**(18), 1610–1612 (2002).
57. M. Yamanari, M. Miura, S. Makita, T. Yatagai, and Y. Yasuno, "Phase retardation measurement of retinal nerve fiber layer by polarization-sensitive spectral-domain optical coherence tomography and scanning laser polarimetry," J. Biomed. Opt. **13**(1), 014013 (2008).
58. S. Zotter, M. Pircher, E. Götzinger, T. Torzicky, H. Yoshida, F. Hirose, S. Holzer, J. Kroisamer, C. Vass, U. Schmidt-Erfurth, and C. K. Hitzenberger, "Measuring Retinal Nerve Fiber Layer Birefringence, Retardation, and Thickness Using Wide-Field, High-Speed Polarization Sensitive Spectral Domain OCT," Invest. Ophthalmol. Visual Sci. **54**(1), 72–84 (2013).
59. J. J. Weiter, F. C. Delori, G. L. Wing, and K. A. Fitch, "Retinal pigment epithelial lipofuscin and melanin and choroidal melanin in human eyes," Invest. Ophthalmol. Vis. Sci. **27**, 145–152 (1986).
60. N. Lippok, B. Braaf, M. Villiger, W.-Y. Oh, B. J. Vakoc, and B. E. Bouma, "Quantitative depolarization measurements for fiber-based polarization-sensitive optical frequency domain imaging of the retinal pigment epithelium," J. Biophotonics **12**(1), e201800156 (2019).
61. C. N. Keilhauer and F. C. Delori, "Near-Infrared Autofluorescence Imaging of the Fundus: Visualization of Ocular Melanin," Invest. Ophthalmol. Visual Sci. **47**(8), 3556–3564 (2006).
62. S. Liakopoulos, S. Ongchin, A. Bansal, S. Msutta, A. C. Walsh, P. G. Updike, and S. R. Sadda, "Quantitative Optical Coherence Tomography Findings in Various Subtypes of Neovascular Age-Related Macular Degeneration," Invest. Ophthalmol. Visual Sci. **49**(11), 5048–5054 (2008).
63. F. C. DeCroos, C. A. Toth, S. S. Stinnett, C. S. Heydary, R. Burns, and G. J. Jaffe, "Optical Coherence Tomography Grading Reproducibility during the Comparison of Age-related Macular Degeneration Treatments Trials," Ophthalmology **119**(12), 2549–2557 (2012).
64. B. Baumann, S. O. Baumann, T. Konegger, M. Pircher, E. Götzinger, F. Schlanitz, C. Schütze, H. Sattmann, M. Litschauer, U. Schmidt-Erfurth, and C. K. Hitzenberger, "Polarization sensitive optical coherence tomography of melanin provides intrinsic contrast based on depolarization," Biomed. Opt. Express **3**(7), 1670–1683 (2012).
65. F. G. Schlanitz, B. Baumann, T. Spalek, C. Schütze, C. Ahlers, M. Pircher, E. Götzinger, C. K. Hitzenberger, and U. Schmidt-Erfurth, "Performance of Automated Drusen Detection by Polarization-Sensitive Optical Coherence Tomography," Invest. Ophthalmol. Visual Sci. **52**(7), 4571–4579 (2011).
66. C. Schütze, M. Wedl, B. Baumann, M. Pircher, C. K. Hitzenberger, and U. Schmidt-Erfurth, "Progression of Retinal Pigment Epithelial Atrophy in Antiangiogenic Therapy of Neovascular Age-Related Macular Degeneration," Am. J. Ophthalmol. **159**(6), 1100–1114.e1 (2015).
67. B. Baumann, J. Schirmer, S. Rauscher, S. Fialová, M. Glösmann, M. Augustin, M. Pircher, M. Gröger, and C. K. Hitzenberger, "Melanin Pigmentation in Rat Eyes: In Vivo Imaging by Polarization-Sensitive Optical Coherence Tomography and Comparison to Histology," Invest. Ophthalmol. Visual Sci. **56**(12), 7462–7472 (2015).
68. A. S. Willoughby, G.-s. Ying, C. A. Toth, M. G. Maguire, R. E. Burns, J. E. Grunwald, E. Daniel, and G. J. Jaffe, Comparison of Age-Related Macular Degeneration Treatments Trials Research Group, "Subretinal hyperreflective material in the comparison of age-related macular degeneration treatments trials," Ophthalmology **122**(9), 1846–1853.e5 (2015).
69. K. K. Dansingani, A. C. S. Tan, F. Gilani, N. Phasukkijwatana, E. Novais, L. Querques, N. K. Waheed, J. S. Duker, G. Querques, L. A. Yannuzzi, D. Sarraf, and K. B. Freund, "Subretinal hyperreflective material imaged with optical coherence tomography angiography," Am. J. Ophthalmol. **169**, 235–248 (2016).
70. Y. Kawashima, M. Hata, A. Oishi, S. Ooto, K. Yamashiro, H. Tamura, M. Miyata, A. Uji, N. Ueda-Arakawa, and A. Tsujikawa, "Association of vascular versus avascular subretinal hyperreflective material with aflibercept response in age-related macular degeneration," Am. J. Ophthalmol. **181**, 61–70 (2017).

Biomedical Optics EXPRESS

71. S. G. Schuman, A. F. Koreishi, S. Farsiu, S. H. Jung, J. A. Izatt, and C. A. Toth, "Photoreceptor Layer Thinning over Drusen in Eyes with Age-Related Macular Degeneration Imaged In Vivo with Spectral-Domain Optical Coherence Tomography," Ophthalmology **116**(3), 488–496.e2 (2009).
72. Y. Ouyang, F. M. Heussen, A. Hariri, P. A. Keane, and S. R. Sadda, "Optical Coherence Tomography–Based Observation of the Natural History of Drusenoid Lesion in Eyes with Dry Age-related Macular Degeneration," Ophthalmology **120**(12), 2656–2665 (2013).
73. J. G. Christenbury, F. A. Folgar, R. V. O'Connell, S. J. Chiu, S. Farsiu, and C. A. Toth, "Progression of Intermediate Age-related Macular Degeneration with Proliferation and Inner Retinal Migration of Hyperreflective Foci," Ophthalmology **120**(5), 1038–1045 (2013).
74. F. G. Schlanitz, S. Sacu, B. Baumann, M. Bolz, M. Platzer, M. Pircher, C. K. Hitzenberger, and U. Schmidt-Erfurth, "Identification of Drusen Characteristics in Age-Related Macular Degeneration by Polarization-Sensitive Optical Coherence Tomography," Am. J. Ophthalmol. **160**(2), 335–344.e1 (2015).